Imaging of Single-Photon Orbital-Angular-Momentum Bell States

Xiao-Xiao Chen,[†] Qing-Yuan Wu,[†] Zhe Meng, Mairikena Aili, Jian Li, Jia-Zhi Yang, and An-Ning Zhang[*]

Center for Quantum Technology Research and Key Laboratory of Advanced Optoelectronic Quantum Architecture and Measurements (MOE), School of Physics, Beijing Institute of Technology, Haidian District, Beijing 100081, People's Republic of China

(Received 23 March 2022; revised 8 September 2022; accepted 7 October 2022; published 17 November 2022)

Bell states are the most fundamental resource in realizing quantum information tasks and have a very unique position in quantum mechanics. Utilizing orbital angular momentum (OAM) to encode single-photon Bell states enables the realization of high-dimensional Hilbert space, which is crucial for the field of quantum information. In this paper, we design a single-photon OAM Bell-state evolution device based on the Sagnac interferometer, which can make one-to-one correspondence between the input Bell states and the output states. Moreover, we also develop a single-photon single-pixel imaging (SPI) technique, which improves spatial resolution and decreases acquisition time in the meantime, to capture interference images of output states. The results show that single-photon OAM Bell states can be fully recognized by comparing the differences of interference images. We innovatively utilize the SPI technique for single-photon OAM Bell-state recognition. This indicates that the SPI technique effectively promotes the study of quantum information based on OAM, while the quantum information based on OAM provides a clear application scenario for the SPI technique.

DOI: 10.1103/PhysRevApplied.18.054053

I. INTRODUCTION

Quantum entanglement was described by Einstein as spooky action at a distance [1]. It is not only a unique property of quantum mechanics, but also a core resource in quantum information [2]. Bell states, as the largest entangled states in a two-qubit system, have been extensively studied since it was proposed. The most common standard Bell states are two-qubit Bell states of two photons in an optics system [3–5]. In 2001, Zeilinger *et al*. proposed multidimensional entanglement as a way—in addition to multiparticle entanglement—to extend the usual two-dimensional two-particle state [6]. Therefore, it has given rise to other forms of Bell states—single-photon two-qubit Bell states, such as, single-photon polarization-path Bell states [7–10], etc.

Orbital angular momentum (OAM) [11,12], as an alternative photon degree of freedom (DOF), has been widely applied in the field of quantum information. For example, a number of studies have emerged that utilize OAM to encode two-qubit Bell states in recent years [13–17]. Since OAM of photons has high-dimensional characteristics [18], using OAM to encode Bell states not merely realizes a high-dimensional Hilbert space, but also enhances the ability of quantum states to carry information. Of note, the measurement of the OAM Bell states is required when the information is finally decoded. The measurement of the single-photon OAM Bell states has been achieved in the previous experiments [16,17], which converted OAM modes to the fundamental Gaussian mode. Due to the infinite dimensions of OAM, the previous method of measuring OAM may not be able to detect the information of all OAM modes in the system, resulting in information loss. By contrast, the single-photon imaging (SPI) technique can measure multiple OAM modes by measuring the spatial distribution of single-photon OAM, so as to obtain more complete information. But as the order of photonic OAM increases, the more complex the images are, the higher the spatial resolution (SR) is required. Therefore, imaging techniques with as high SR as possible are required to realize the discrimination of high-order OAM images. The SPI [19–21], which uses dynamic illumination to obtain spatial information, is an innovative scheme and has received increasing attention recently. It is capable of imaging under low-light conditions [22–26]. And its SR is limited only by the spatial light modulator, making it a potential candidate for obtaining high-SR OAM images [27]. Unfortunately, SPI requires continuous measurements, resulting in a trade-off between SR and acquisition time [25,27,28]. Hence, the requirement to achieve high-SR and low acquisition time at the same time is a bottleneck of SPI.

[*]Corresponding author. Anningzhang@bit.edu.cn
[†]These authors contributed equally to this work.

In this paper, we design a single-photon OAM Bell-state evolution device based on the Sagnac interferometer, which can make one-to-one correspondence between the input single-photon OAM Bell states and the output states. Furthermore, we develop a quick-sort Hadamard SPI technique—based on compressed sensing to improve SR and decrease acquisition time at the same time—to capture interference images of output states. Then utilizing the proposed imaging technique, we experimentally demonstrate the interference images of four output states, which are shown to be different from each other. The results show that by comparing the differences of these interference images, we can realize complete Bell-state recognition. In addition, we experimentally show a set of interference images with high enough SR (256×256 pixels). In our opinion, this research is at the cross field of quantum information and quantum imaging. The application of the SPI technique in the quantum information field and the experimental research of quantum information based on SPI are helpful to promote the development of quantum information science and technology.

II. THEORY AND METHODS

We define the four single-photon two-qubit Bell states with OAM and polarization DOFs,

$$\begin{aligned} |\Psi^{\pm}\rangle &= \frac{1}{\sqrt{2}}(|H,m\rangle \pm |V,-m\rangle), \\ |\Phi^{\pm}\rangle &= \frac{1}{\sqrt{2}}(|H,-m\rangle \pm |V,m\rangle), \end{aligned} \tag{1}$$

where $|H\rangle$ and $|V\rangle$ represent the horizontal and vertical polarizations of the photons. $|\pm m\rangle$ represent the photons with OAM of $\pm m\hbar$, and m is called the topological charge. In recent years, the methods used to generate OAM include spiral phase plate (SPP) [29,30], hologram [31,32], q plate [33] or vortex wave-plate (VWP) [34], etc. Here, we utilize VWP to prepare the above single-photon OAM Bell states. Figure 1(a) is the schematic of preparing single-photon OAM Bell states using VWP. Take the preparation of the single-photon OAM Bell state $|\Psi^{+}\rangle$ as an example, the specific preparation details are as follows (the input is H-polarized Gaussian light, whose photons state is $|H,0\rangle$).

$$\begin{aligned} |H,0\rangle &\xrightarrow{\text{HWP}(45^\circ)} |V,0\rangle \xrightarrow{\text{QWP1}(0^\circ)} i|V,0\rangle = \frac{1}{\sqrt{2}}(|R,0\rangle \\ &- |L,0\rangle) \xrightarrow{\text{VWP}(m)} \frac{1}{\sqrt{2}}(|L,m\rangle - |R,-m\rangle) \xrightarrow{\text{QWP2}(-45^\circ)} \\ &= \frac{1}{\sqrt{2}}(|H,m\rangle - |iV,-m\rangle) \xrightarrow{\text{QWP3}(0^\circ)} \frac{1}{\sqrt{2}} \\ &\times (|H,m\rangle + |V,-m\rangle) \\ &= \left|\Psi^{+}\right\rangle. \end{aligned} \tag{2}$$

Here, the function of m-order VWP is described as $|R,m'\rangle \xrightarrow{m\text{ order}} |L,m'+m\rangle$; $|L,m'\rangle \xrightarrow{m\text{ order}} |R,m'-m\rangle$, where, $|R\rangle \propto |H\rangle + i|V\rangle$ and $|L\rangle \propto |H\rangle - i|V\rangle$ represent the right- and left-circularly polarized states, respectively. The other three OAM Bell states are prepared in a similar way, details can be found in Appendix A.

As shown in Fig. 1(b), we design a OAM Bell-state evolution device based on the Sagnac interferometer, which can make each OAM Bell state correspond to a unique output state. Its principle is as follows: input state $|\Psi^{+}\rangle = 1/\sqrt{2}(|H,m\rangle + |V,-m\rangle)$, for example, after polarization beam splitter (PBS), this state will be decomposed into $1/\sqrt{2}|H,m\rangle$ in the transmission direction and $1/\sqrt{2}|V,m\rangle$ in the reflection direction. Note that the sign of topological charge in the reflection direction is changed because the reflection effect reverses the sign of topological charge [35]. Then, the transmitted part passes through mirror 1 (M1), M2, phase controller (PC), and M3 in turn. Instead, the reflected part passes through M3, PC, M2, and M1 in turn. Specifically, $1/\sqrt{2}|H,m\rangle \xrightarrow{\text{M1}} 1/\sqrt{2}|H,-m\rangle \xrightarrow{\text{M2}} 1/\sqrt{2}|H,m\rangle \xrightarrow{\text{PC}} 1/(\sqrt{2})e^{i\theta}|H,m\rangle \xrightarrow{\text{M3}} 1/(\sqrt{2})e^{i\theta}|H,-m\rangle$; $1/\sqrt{2}|V,m\rangle \xrightarrow{\text{M3}} 1/\sqrt{2}|V,-m\rangle \xrightarrow{\text{PC}} 1/\sqrt{2}|V,-m\rangle \xrightarrow{\text{M2}} 1/\sqrt{2}|V,m\rangle \xrightarrow{\text{M1}} 1/\sqrt{2}|V,-m\rangle$. It is worthwhile to point out that the phase $e^{i\theta}$ is controlled by the PC; the function of which is only to add the phase to $|H\rangle$ polarization. After the interference loop evolution, the two partial states will remeet at PBS and leave at another port, and the state is $1/(\sqrt{2})e^{i\theta}|H,-m\rangle + 1/\sqrt{2}|V,m\rangle$. This is the output state of the state $|\Psi^{+}\rangle$ after the Sagnac interferometer evolution. After passing through the Sagnac interferometer, the photons are divided into two detectors by 22.5° HWP and PBS (not plotted in Fig. 1). The evolution of this step is $1/(\sqrt{2})e^{i\theta}|H,-m\rangle + 1/\sqrt{2}|V,m\rangle \xrightarrow{\text{HWP}(22.5^\circ)+\text{PBS}} 1/2(e^{i\theta}|-m\rangle + |m\rangle)_T|H\rangle_T + 1/2(e^{i\theta}|-m\rangle - |m\rangle)_R|V\rangle_R$. Here, the subscript $T(R)$ denotes the transmitted (reflected) part of PBS. Here, we consider only the transmission part

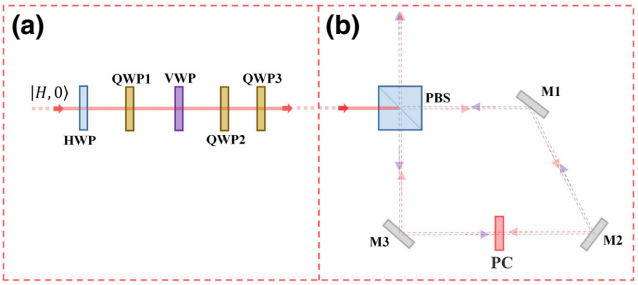

FIG. 1. (a) Schematic of preparing single-photon OAM Bell states. HWP, half-wave plate; QWP, quarter-wave plate; VWP, vortex wave plate. (b) Single-photon OAM Bell-state evolution device. The dashed lines and arrows indicate only the light-propagation direction. PBS, polarization beam splitter; M, mirror; PC, phase controller.

of PBS. Eventually, the state $|\Psi^+\rangle$ will correspond to a output state, i.e., $|\Psi^+\rangle \rightarrow |\Psi^+\rangle' = 1/2(e^{i\theta}|-m\rangle + |m\rangle)$. The corresponding output states of the four OAM Bell states are (details of the evolution of the other three states can be found in Appendix B).

$$\begin{aligned}
|\Psi^+\rangle &\rightarrow |\Psi^+\rangle' = \frac{1}{2}(e^{i\theta}|-m\rangle + |m\rangle),\\
|\Psi^-\rangle &\rightarrow |\Psi^-\rangle' = \frac{1}{2}(e^{i\theta}|-m\rangle - |m\rangle),\\
|\Phi^+\rangle &\rightarrow |\Phi^+\rangle' = \frac{1}{2}(e^{i\theta}|m\rangle + |-m\rangle),\\
|\Phi^-\rangle &\rightarrow |\Phi^-\rangle' = \frac{1}{2}(e^{i\theta}|m\rangle - |-m\rangle).
\end{aligned} \tag{3}$$

The interference results of above output states carrying opposite-sign ($\pm m$) OAM is a petal-like light spot, and the number of petals is $2m$ [35]. Furthermore, these output states are related to phase $e^{i\theta}$, which results in the rotation of the petal-like light spot, where $\theta \in [0, 2\pi]$ is the phase shifted by the PC. So for a given θ, we can obtain the interference images corresponding to the four output states. Because there is a one-to-one correspondence between the single-photon OAM Bell states and the output states, we can recognize which Bell state is the input based on the differences of interference images. The whole process above is what we call Bell-state recognition.

Figure 2 shows the simulation diagram of the four output states in Eq. (3). The interference images for four output states correspond to four different petal images. To illustrate how these petal images are different, we define the angular position φ of the petal of output state $|\Psi^+\rangle'$, and use it as the reference standard. For output state $|\Psi^+\rangle'$, there is a relationship between φ and θ, $\varphi = \theta/2m$ [35], where $\varphi_{m=1} \in [0, \pi]$, $\varphi_{m=2} \in [0, \pi/2]$, $\varphi_{m=3} \in [0, \pi/3]$. As shown in the first column of Fig. 1, when $\theta = 7\pi/4$, $\varphi_{|\Psi^+\rangle'(m=1)} = 7\pi/8$, $\varphi_{|\Psi^+\rangle'(m=2)} = 7\pi/16$, $\varphi_{|\Psi^+\rangle'(m=3)} = 7\pi/24$. As shown in Fig. 1, the angular positions φ of the petals in columns 2, 3, and 4 are rotated to different angles with respect to column 1, respectively. Specifically, when $m = 1$, $\varphi_{|\Psi^-\rangle'} - \varphi_{|\Psi^+\rangle'} = 4\pi/8$, $\varphi_{|\Phi^+\rangle'} - \varphi_{|\Psi^+\rangle'} = -6\pi/8$, $\varphi_{|\Phi^-\rangle'} - \varphi_{|\Psi^+\rangle'} = -2\pi/8$; when $m = 2$, $\varphi_{|\Psi^-\rangle'} - \varphi_{|\Psi^+\rangle'} = 4\pi/16$, $\varphi_{|\Phi^+\rangle'} - \varphi_{|\Psi^+\rangle'} = -6\pi/16$, $\varphi_{|\Phi^-\rangle'} - \varphi_{|\Psi^+\rangle'} = -2\pi/16$; when $m = 3$, $\varphi_{|\Psi^-\rangle'} - \varphi_{|\Psi^+\rangle'} = 4\pi/24$, $\varphi_{|\Phi^+\rangle'} - \varphi_{|\Psi^+\rangle'} = -6\pi/24$, $\varphi_{|\Phi^-\rangle'} - \varphi_{|\Psi^+\rangle'} = -2\pi/24$. According to the above formulas, we can know that when m is fixed, the corresponding φ values of the four output states are different. Therefore, the differences of these images are characterized by these angular positions φ of the petals. Then, we can completely (that is 100% efficiency) recognize the OAM Bell states based on the differences in the interference images of the four output states.

In Fig. 2, we simulate only the three cases $m = 1, 2, 3$. Due to the infinite dimension property of OAM, m can take an arbitrarily large integer. According to $\varphi = \theta/2m$, however, $\Delta\varphi = \Delta\theta/2m$ can obtained, where $\Delta\theta$ is phase difference, $\Delta\varphi$ is the angular positions' difference of the petals. Figure 3 shows our simulation results between m and $\Delta\varphi$ for $|\Psi^+\rangle'$. When $\Delta\theta = \pi/4$, $\Delta\varphi_{m=1} = \pi/8$, $\Delta\varphi_{m=2} = \pi/16$, $\Delta\varphi_{m=3} = \pi/24$ (this result also holds for the other three output states). It shows that when $\Delta\theta$ is fixed, the larger the values of m, the smaller the the angular positions' difference of the petals $\Delta\varphi$. Unfortunately, when $\Delta\varphi$ is small enough, all petal boundaries become blurred for low spatial resolution (SR) images. This situation is not conducive to using the angular positions of the petals to distinguish the differences between the images. In contrast, images with high SR will effectively alleviate this

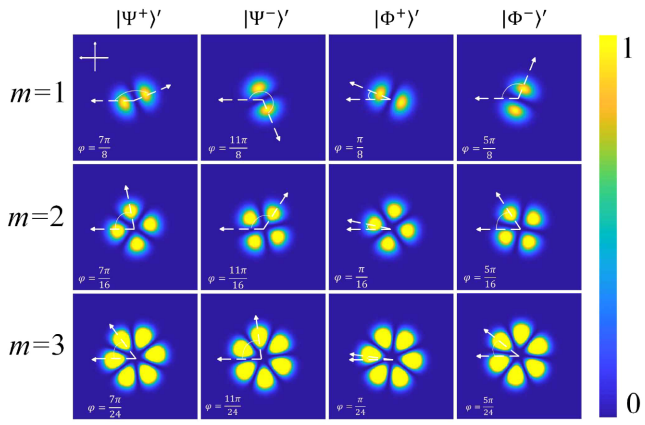

FIG. 2. Simulation images of the four output states, $\theta = \frac{7\pi}{4}$. The values of angles φ are shown in the bottom left corner, in the figure the angular positions of the petals that we define in main text are shown.

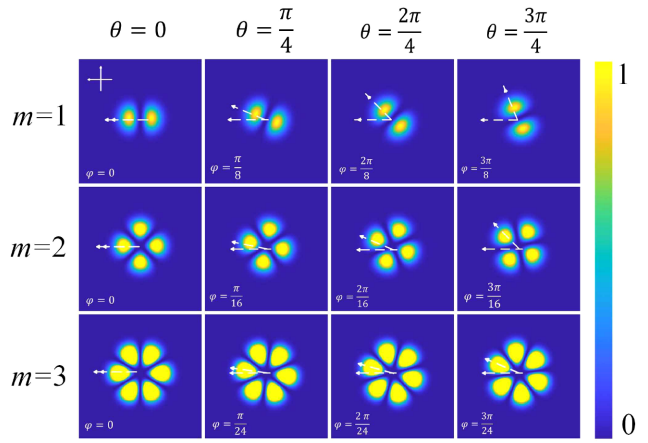

FIG. 3. Simulation results between order m and $\Delta\varphi$ for $|\Psi^+\rangle'$. For example, when $\Delta\theta = \frac{\pi}{4}$, $\Delta\varphi_{m=1} = \varphi_{(\theta=\frac{\pi}{4})} - \varphi_{(\theta=0)} = \frac{\pi}{8}$, $\Delta\varphi_{m=2} = \varphi_{(\theta=\frac{\pi}{4})} - \varphi_{(\theta=0)} = \frac{\pi}{16}$, $\Delta\varphi_{m=1} = \varphi_{(\theta=\frac{\pi}{4})} - \varphi_{(\theta=0)} = \frac{\pi}{24}$.

situation. From this point of view, high SR is necessary for the recognition of high-order OAM Bell states.

We intend to utilize the single-photon single-pixel imaging technique to recognize single-photon OAM Bell states. However, SPI requires continuous measurement of the target, resulting in a trade-off between SR and acquisition time. The compressed sensing techniques are used to mitigate the trade-off. The proposed optimized methods of Hadamard SPI, including Russian-doll (RD) order [28] and cake-cutting (CC) order [36]. However, the RD order is limited by high computational complexity, so it can only sort patterns whose SR is less than 128×128 pixels; the CC order is limited by the calculation method, only one sorting method can be provided, and there is no clear calculation formula. In this study, we demonstrate a sort-based Hadamard SPI scheme that uses an efficient and easy-to-implement sampling method based on the Hadamard patterns to achieve fast high-SR imaging. We call it the quick-sort Hadamard SPI scheme (see Appendix C for details).

III. EXPERIMENTAL SETUP

We now demonstrate the experimental implementation of single-photon OAM Bell-state recognition. As shown in Fig. 4, the whole experimental device consists of single-photon source preparation, single-photon OAM Bell-state preparation and evolution, and SPI device. The method of preparing single-photon source is the same as Refs. [8,37]. As shown in Fig. 4(a), the pump light is a fundamental-mode Gaussian cw diode laser with a power of 20 mW and a central wavelength of 405 nm. It pumps type-II phase-matched periodically poled potassium titanyl phosphate (PPKTP) crystal and generates an entangled photon pair at 810 nm based on spontaneous parametric down-conversion (SPDC). Then, the photon pair is split into two arms at PBS1, and the detection of a V polarization photon at avalanche photodiodes 0 (APD0) indicates a H polarization photon along the other arm. In order to characterize the performance of the single-photon source, we measure the value of the second-order correlation function $g^{(2)}$ as 0.0236.

The single-photon source is connected to the single-photon OAM Bell-state preparation and evolution section using SMF. As shown in Fig. 4(b), PBS3 is used as the inlet and outlet of the device. It divides the incident light beam into horizontally polarized light beam along clockwise and vertically polarized light beam along counterclockwise, respectively. After being successively reflected by mirrors, they regroup again and exit the interferometer from the other end of PBS3. The liquid crystal (LC) is inserted into the interferometer; the function of which is to add a phase to the H polarization state without changing the sign of the OAM. However, the holistic setup changes the sign of the

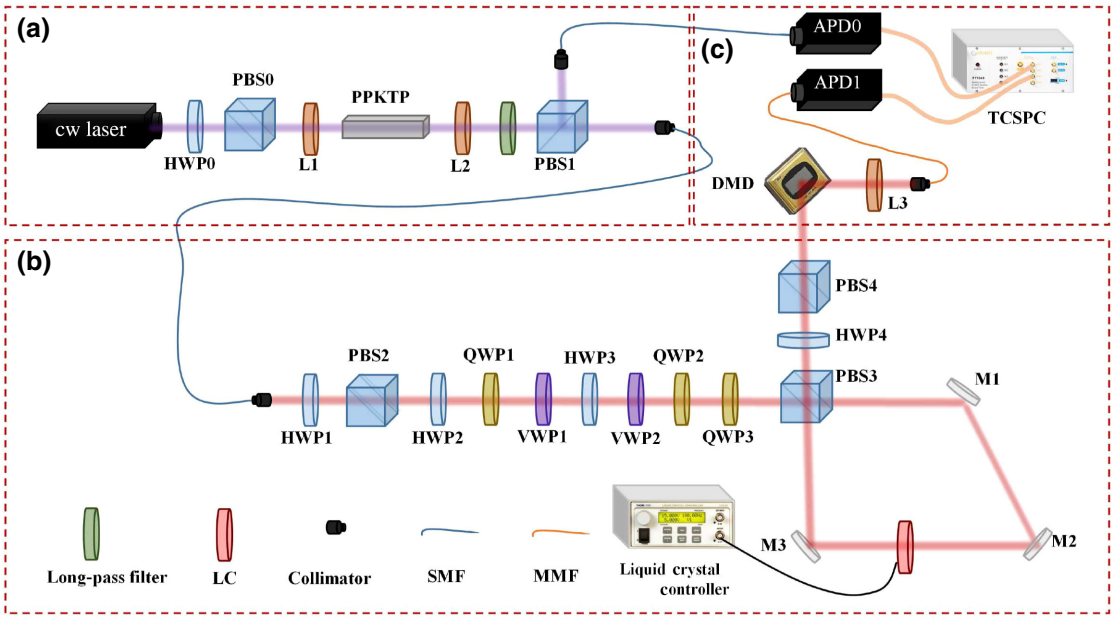

FIG. 4. Experimental setup for single-photon OAM Bell-state recognition. (a) Single-photon source preparation. A 405-nm cw diode laser with 20-mW power pumps a periodically poled potassium titanyl phosphate PPKTP crystal to produce photon pairs with central wavelength of 810 nm based on SPDC. (b) Single-photon OAM Bell-state preparation and evolution. Here, the order of VWP1 and VWP2 are $m = 1$ and $m = 2$, respectively. HWP3 and VWP2 are only needed to prepare the OAM state with $m = 3$. (c) Single-pixel imaging device. The imaging device is composed of DMD, lens, APDs, and TCSPC. Patterns are loaded on the DMD. DMD reflects photon states to APD1 for collection. Finally, the quick-sort Hadamard SPI scheme is used to reconstruct OAM Bell-state images. It should be noted that our DMD is tilted 45° for convenience. MMF, multimode fiber.

OAM because the total number of mirrors and PBS is odd for both polarizations. As shown in Fig. 4(b), when HWP4 is 22.5° and $|D\rangle \propto |H\rangle + |V\rangle$ is taken as the measurement base, we choose to conduct detection at the transmission end of PBS4.

Notably, we do not convert OAM modes to the fundamental Gaussian mode. Due to the infinite dimensions of OAM, the previous method of measuring OAM using a spatial single-mode optical device has some shortcomings. The previous method converts only the OAM order concerned in the experiment into the fundamental mode for measurement, and may not be able to detect the information of all OAM modes in the system, resulting in information loss. In contrast, we use the imaging method to measure the photon distribution in the whole space, which can be more comprehensive and intuitive to obtain all information. The evolved photons of the four single-photon OAM Bell states are emitted from the same end of PBS4 and directly received by the SPI device for imaging, as shown in Fig. 4(c). The SPI device contains a digital mirror device (DMD), lens, APDs, and time-correlated single-photon counting (TCSPC). The DMD, which contains 1024 × 768 micromirrors and each pixel is 13.68 μm, is illuminated by photons emanating from PBS4 and operates at a refresh rate of 0.1Hz. Photons emanating from PBS4 are reflected by the Hadamard pattern displayed on DMD and collected by APD1 after passing through a lens. The role of TCSPC is to convert light-intensity signals into digital signals.

IV. RESULTS AND DISCUSSION

To test the performance of the quick-sort Hadamard SPI scheme, some numerical simulations are performed (see Appendix D for details). In addition, we conduct experimental verification on the simulation diagram of Fig. 2, and

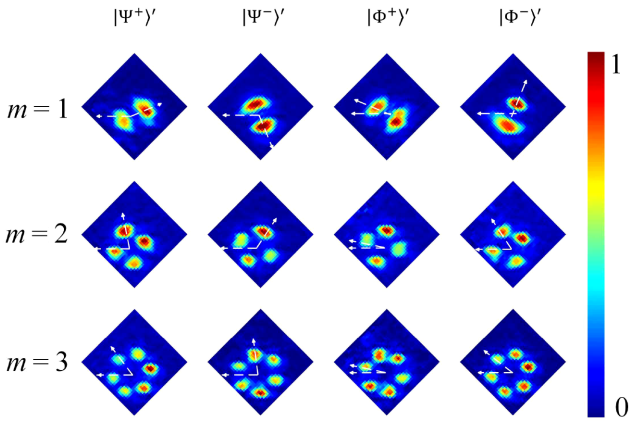

FIG. 5. Experimental results correspond to the simulation diagram of Fig. 1. Patterns of 32 × 32 pixels are sorted that used to measure the output states, which corresponds to the single-photon OAM Bell states with phase $\theta = \frac{7\pi}{4}$.

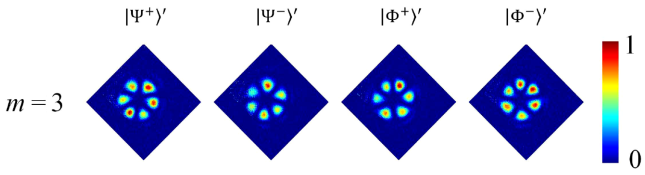

FIG. 6. High-SR images are reconstructed using patterns sorted by quick-sort Hadamard SPI. In the case of $m = 3$ and phase $\theta = \frac{\pi}{4}$, the images (256 × 256 pixels) of the output states correspond to the single-photon OAM Bell states.

the results are shown in Fig. 5. It is necessary to state that we perform a proof-of-principle experiment. In order to qualitatively characterize the degree of agreement between experiment and theory, in Fig. 5, we mark the angular positions φ of petals, which are theoretical values and exactly the same as in Fig. 2. According to Fig. 5, the angular positions of the petals of each output state are in good agreement with the theory. One of the main reasons for the difference between experiment and theory is that the current imaging quality is not good enough, so we should develop high-quality single-photon imaging technology.

The above experimental results are all low-SR images (32 × 32 pixels). For low-order OAM images ($m = 1, 2, 3$), it can clearly see the difference of the angular positions of petals. However, for high-order OAM, high-SR images are required to allow for accurate discrimination. As shown in Fig. 6, this is the experimental results of 256 × 256 pixels obtained by using our proposed quick-sort Hadamard SPI scheme. Compared with the third row of Fig. 5, the petals' shape in Fig. 6 is more regular, and the boundary of the petals are also clearer. This result shows that high-SR images are more suitable for the recognition of high-order OAM images than low-SR images. Although we show only high-SR images for $m = 3$, we theoretically calculate that the highest OAM order that can be resolved by 256 × 256 pixels is $m = 300$, while the highest OAM order that can be distinguished by 32 × 32 pixels is only $m = 12.5$ because of the minimum angle that can be resolved by each digital image is limited theoretically.

V. CONCLUSIONS

In conclusion, we present a scheme for the preparation, evolution, and measurement of single-photon OAM Bell states in a Hilbert space composed of polarization and OAM using a simple unitary operation of linear optics. In order to obtain images of the output states corresponding to the OAM Bell states, we develop the quick-sort Hadamard SPI scheme based on a trade-off between SR and acquisition time. Experimentally, we use the proposed SPI scheme to display interference images with different output states. By comparing the differences of these interference images, we achieve complete Bell-state recognition. For traditional Bell-state measurement, the input state is an

arbitrary polarization state and the Bell-state measurement can distinguish all four orthogonal Bell states. Our Bell-state recognition technique is different from the traditional Bell-state measurement. Our technique can recognize Bell states (that is the input state are Bell states), but it cannot use the discriminating information in quantum protocols. And we are still working on how to use our recognizing information in quantum protocols. By demonstrating that quick-sort Hadamard SPI can generate OAM images to achieve Bell-state recognition, we combine quantum imaging technology with the most fundamental quantum information problems. This combination not only opens the way for a quantum imaging scheme based on Bell-state recognition, but also expands the application range of SPI.

ACKNOWLEDGMENTS

We are grateful to Professor Qing Zhao for helpful discussions and experimental help. This work is supported by National Key Research and Development Program Earth Observation and Navigation Key Specialities (No. 2018YFB0504300).

APPENDIX A: SINGLE-PHOTON OAM BELL-STATE PREPARATION

As shown in Fig. 7(a), we use VWP to generate OAM to prepare the single-photon OAM Bell states. The VWP (m-order), which is used to transform the fundamental Gaussian mode state $|0\rangle$ into the OAM state $|+m\rangle$ or $|-m\rangle$. In general, the function of m-order VWP is described as

$$\begin{aligned} |R,m'\rangle &\xrightarrow{m\text{ order}} |L,m'+m\rangle, \\ |L,m'\rangle &\xrightarrow{m\text{ order}} |R,m'-m\rangle. \end{aligned} \tag{A1}$$

Here, $|R\rangle \propto |H\rangle + i|V\rangle$ and $|L\rangle \propto |H\rangle - i|V\rangle$ represent the right- and left-circularly polarized states, respectively. We show the preparation of the $|\Psi^+\rangle$ state in the main text, and we focus on the preparation of the other three too below. Note that the input is H-polarized Gaussian light, whose photons' state is $|H,0\rangle$. The specific process of preparing the $|\Psi^-\rangle$ state is as follows:

$$\begin{aligned} |H,0\rangle &\xrightarrow{\text{HWP1}(0^\circ)} |H,0\rangle \xrightarrow{\text{QWP1}(0^\circ)} |H,0\rangle = \frac{1}{\sqrt{2}}(|R,0\rangle \\ &+ |L,0\rangle) \xrightarrow{\text{VWP}(m)} \frac{1}{\sqrt{2}}(|L,m\rangle + |R,-m\rangle) \xrightarrow{\text{QWP2}(-45^\circ)} \\ &= \frac{1}{\sqrt{2}}(|H,m\rangle + |iV,-m\rangle) \xrightarrow{\text{QWP3}(0^\circ)} \frac{1}{\sqrt{2}} \\ &\times (|H,m\rangle - |V,-m\rangle) = \left|\Psi^-\right\rangle. \end{aligned} \tag{A2}$$

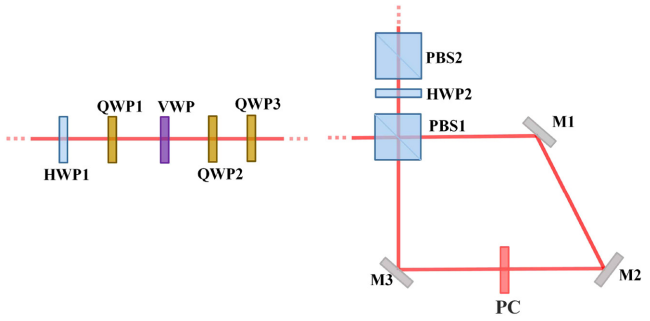

FIG. 7. (a) Schematic of preparing single-photon OAM Bell states. (b) Single-photon OAM Bell-state evolution device. HWP, half-wave plate; QWP, quarter-wave plate; VWP, vortex wave plate; PBS, polarization beam splitter; M, mirror; PC, phase controller.

The specific process of preparing the $|\Phi^+\rangle$ state is as follows:

$$\begin{aligned} |H,0\rangle &\xrightarrow{\text{HWP1}(0^\circ)} |H,0\rangle \xrightarrow{\text{QWP1}(0^\circ)} |H,0\rangle = \frac{1}{\sqrt{2}}(|R,0\rangle \\ &+ |L,0\rangle) \xrightarrow{\text{VWP}(m)} \frac{1}{\sqrt{2}}(|L,m\rangle + |R,-m\rangle) \xrightarrow{\text{QWP2}(45^\circ)} \\ &= \frac{1}{\sqrt{2}}(|H,-m\rangle - |iV,m\rangle) \xrightarrow{\text{QWP3}(0^\circ)} \frac{1}{\sqrt{2}} \\ &\times (|H,-m\rangle + |V,m\rangle) = \left|\Phi^+\right\rangle. \end{aligned} \tag{A3}$$

The specific process of preparing the $|\Phi^-\rangle$ state is as follows:

$$\begin{aligned} |H,0\rangle &\xrightarrow{\text{HWP1}(-45^\circ)} -|V,0\rangle \xrightarrow{\text{QWP1}(0^\circ)} -i|V,0\rangle = \frac{1}{\sqrt{2}} \\ &(-|R,0\rangle + |L,0\rangle) \xrightarrow{\text{VWP}(m)} \frac{1}{\sqrt{2}}(-|L,m\rangle + |R,-m\rangle) \\ &\xrightarrow{\text{QWP2}(45^\circ)} = \frac{1}{\sqrt{2}}(|H,-m\rangle + |iV,m\rangle) \xrightarrow{\text{QWP3}(0^\circ)} \\ &\frac{1}{\sqrt{2}}(|H,-m\rangle - |V,m\rangle) = \left|\Phi^-\right\rangle. \end{aligned} \tag{A4}$$

APPENDIX B: THE EVOLUTION OF SINGLE-PHOTON OAM BELL STATES

As shown in Fig. 7(b), we design a OAM Bell-state evolution device based on the Sagnac interferometer, which can make each OAM Bell state correspond to a unique output state. We already analyze in the main text how the input state $|\Psi^+\rangle$ evolves in the Sagnac interference loop. Therefore, here we present only the evolution of the remaining three OAM Bell states.

First, take $|\Psi^-\rangle$ as input state,

$$\frac{1}{\sqrt{2}}(|H,m\rangle - |V,-m\rangle) \xrightarrow{\text{PBS1}(T)} \frac{1}{\sqrt{2}}|H,m\rangle \xrightarrow{\text{M1}} \frac{1}{\sqrt{2}}$$
$$|H,-m\rangle \xrightarrow{\text{M2}} \frac{1}{\sqrt{2}}|H,m\rangle \xrightarrow{\text{PC}} \frac{1}{\sqrt{2}}e^{i\theta}|H,m\rangle \xrightarrow{\text{M3}} \frac{1}{\sqrt{2}}$$
$$e^{i\theta}|H,-m\rangle; \tag{B1}$$

$$\frac{1}{\sqrt{2}}(|H,m\rangle - |V,-m\rangle) \xrightarrow{\text{PBS1}(R)} -\frac{1}{\sqrt{2}}|V,m\rangle \xrightarrow{\text{M3}} -\frac{1}{\sqrt{2}}$$
$$|V,-m\rangle \xrightarrow{\text{PC}} -\frac{1}{\sqrt{2}}|V,-m\rangle \xrightarrow{\text{M2}} -\frac{1}{\sqrt{2}}|V,m\rangle \xrightarrow{\text{M1}} -\frac{1}{\sqrt{2}}$$
$$|V,-m\rangle, \tag{B2}$$

where T represents the transmission direction of PBS and R represents the reflection direction of PBS. The above two parts meet again at PBS, and the output state is $1/\sqrt{2}(e^{i\theta}|H,-m\rangle - |V,m\rangle)$. After HWP2 (22.5°) and PBS2 transmission, $1/(\sqrt{2})e^{i\theta}|H,-m\rangle - 1/\sqrt{2}|V,m\rangle \xrightarrow{\text{HWP}(22.5^\circ)} 1/\sqrt{2}(e^{i\theta}|-m\rangle - |m\rangle)_T|H\rangle_T + 1/\sqrt{2}(e^{i\theta}|-m\rangle + |m\rangle)_R|V\rangle_R \xrightarrow{\text{PBS2(T)}} 1/\sqrt{2}(e^{i\theta}|-m\rangle - |m\rangle) = |\Psi^-\rangle'$.

Second, take $|\Phi^+\rangle$ as input state,

$$\frac{1}{\sqrt{2}}(|H,-m\rangle + |V,m\rangle) \xrightarrow{\text{PBS1}(T)} \frac{1}{\sqrt{2}}|H,-m\rangle \xrightarrow{\text{M1}} \frac{1}{\sqrt{2}}$$
$$|H,m\rangle \xrightarrow{\text{M2}} \frac{1}{\sqrt{2}}|H,-m\rangle \xrightarrow{\text{PC}} \frac{1}{\sqrt{2}}e^{i\theta}|H,-m\rangle \xrightarrow{\text{M3}} \frac{1}{\sqrt{2}}e^{i\theta}$$
$$|H,m\rangle; \tag{B3}$$

$$\frac{1}{\sqrt{2}}(|H,-m\rangle + |V,m\rangle) \xrightarrow{\text{PBS1}(R)} \frac{1}{\sqrt{2}}|V,-m\rangle \xrightarrow{\text{M3}} \frac{1}{\sqrt{2}}$$
$$|V,m\rangle \xrightarrow{\text{PC}} \frac{1}{\sqrt{2}}|V,m\rangle \xrightarrow{\text{M2}} \frac{1}{\sqrt{2}}|V,-m\rangle \xrightarrow{\text{M1}} \frac{1}{\sqrt{2}}|V,m\rangle. \tag{B4}$$

The above two parts meet again at PBS, and the output state is $1/\sqrt{2}(e^{i\theta}|H,m\rangle + |V,-m\rangle)$. After HWP2 (22.5°) and PBS2 transmission, $1/(\sqrt{2})e^{i\theta}|H,m\rangle + 1/\sqrt{2}|V,-m\rangle \xrightarrow{\text{HWP}(22.5^\circ)} 1/\sqrt{2}(e^{i\theta}|m\rangle + |-m\rangle)_T|H\rangle_T + 1/\sqrt{2}(e^{i\theta}|m\rangle - |-m\rangle)_R|V\rangle_R \xrightarrow{\text{PBS2}(T)} 1/\sqrt{2}(e^{i\theta}|m\rangle + |-m\rangle) = |\Phi^+\rangle'$.

Third, take $|\Phi^-\rangle$ as input state,

$$\frac{1}{\sqrt{2}}(|H,-m\rangle - |V,m\rangle) \xrightarrow{\text{PBS1}(T)} \frac{1}{\sqrt{2}}|H,-m\rangle \xrightarrow{\text{M1}} \frac{1}{\sqrt{2}}$$
$$|H,m\rangle \xrightarrow{\text{M2}} \frac{1}{\sqrt{2}}|H,-m\rangle \xrightarrow{\text{PC}} \frac{1}{\sqrt{2}}e^{i\theta}|H,-m\rangle \xrightarrow{\text{M3}} \frac{1}{\sqrt{2}}$$
$$e^{i\theta}|H,m\rangle; \tag{B5}$$

$$\frac{1}{\sqrt{2}}(|H,-m\rangle - |V,m\rangle) \xrightarrow{\text{PBS1}(R)} -\frac{1}{\sqrt{2}}|V,-m\rangle \xrightarrow{\text{M3}} -\frac{1}{\sqrt{2}}$$
$$|V,m\rangle \xrightarrow{\text{PC}} -\frac{1}{\sqrt{2}}|V,m\rangle \xrightarrow{\text{M2}} -\frac{1}{\sqrt{2}}|V,-m\rangle \xrightarrow{\text{M1}} -\frac{1}{\sqrt{2}}$$
$$|V,m\rangle. \tag{B6}$$

The above two parts meet again at PBS, and the output state is $1/\sqrt{2}(e^{i\theta}|H,m\rangle - |V,-m\rangle)$. After HWP2 (22.5°) and PBS2 transmission, $1/(\sqrt{2})e^{i\theta}|H,m\rangle - 1/\sqrt{2}|V,-m\rangle \xrightarrow{\text{HWP}(22.5^\circ)} 1/\sqrt{2}(e^{i\theta}|m\rangle - |-m\rangle)_T|H\rangle_T + 1/\sqrt{2}(e^{i\theta}|m\rangle + |-m\rangle)_R|V\rangle_R \xrightarrow{\text{PBS2(T)}} 1/\sqrt{2}(e^{i\theta}|m\rangle - |-m\rangle) = |\Phi^-\rangle'$.

APPENDIX C: QUICK-SORT HADAMARD SPI SCHEME

The core of the proposed quick-sort Hadamard SPI scheme is based on the following equation:

$$f_d = \begin{cases} i \times j, d = 0 \\ (i^d + j^d)^{\frac{1}{d}}, d \neq 0 \end{cases}, \tag{C1}$$

where i and j represent the number of sign changes in any row and any column of pattern, respectively. The pattern is obtained by transforming each row of the Hadamard matrix. Constant d is a preset parameter and f_d is the corresponding value of a pattern calculated by Eq. (C1). Finally, we sort the patterns in ascending order of f_d value to obtain quick-sort order. High spatial resolution can improve the distinguishing ability of OAM images. So it is necessary to sort patterns with high spatial resolution. According to our scheme, we can sort patterns of any pixel size. Further, by adjusting the preset parameter d, different orders can be obtained quickly.

Here, Fig. 8 gives an example of how our quick-sort scheme works. The H_{16} matrix [Fig. 8(a)] is generated by computer, and then each row in the matrix is selected and transformed into a series of 4×4 2D patterns. Such a complete natural order 4×4 Hadamard pattern set is obtained, as shown in the first row of Fig. 8(e). According to the proposed scheme, any row of Hadamard matrix is selected and transformed into 2D pattern to count the number of sign changes, as shown in Fig. 8(b). Assuming $d = 0.5$, the f_d value is calculated by Eq. (C1), and then each pattern is sorted according to the ascending order. Figure 8(c) shows the f_d value and position of each pattern in the natural order, and Fig. 8(d) shows the f_d value and new position of each pattern after the ascending order of f_d value. The second to fifth lines of Fig. 8(e) represent the orders of different parameters d.

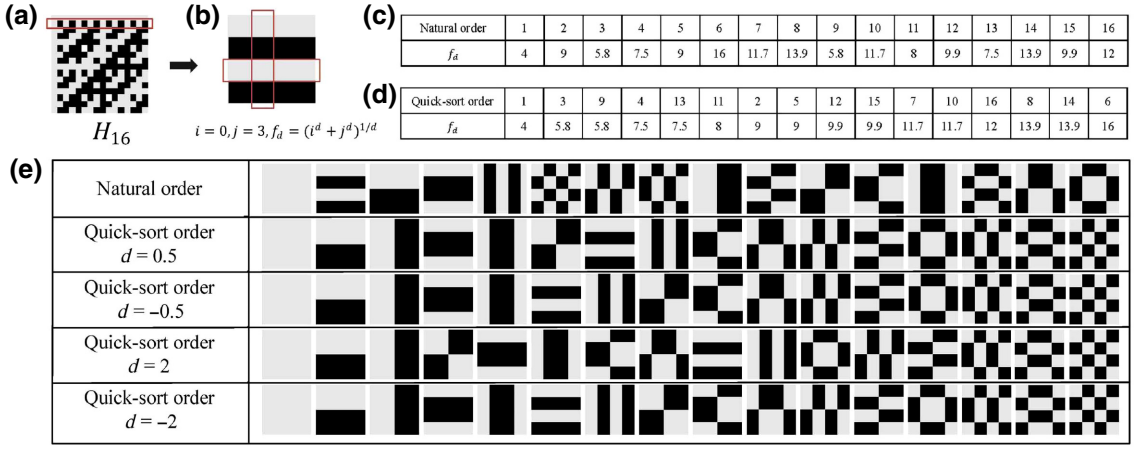

Natural order	1	2	3	4	5	6	7	8	9	10	11	12	13	14	15	16
f_d	4	9	5.8	7.5	9	16	11.7	13.9	5.8	11.7	8	9.9	7.5	13.9	9.9	12

Quick-sort order	1	3	9	4	13	11	2	5	12	15	7	10	16	8	14	6
f_d	4	5.8	5.8	7.5	7.5	8	9	9	9.9	9.9	11.7	11.7	12	13.9	13.9	16

FIG. 8. An example for the quick-sort Hadamard patterns. (a) A 16 × 16 Hadamard matrix H_{16}. (b) A row of the Hadamard matrix in (a) marked by red circles is transformed to a 2D pattern. (c) The patterns of H_{16} in the natural order, the first line is the original position of each pattern and the second line is the corresponding f_d value. (d) The patterns of H_{16} in the quick-sort order in $d = 0.5$, the first line is the new position of each pattern and the second line is the corresponding f_d value. (e) Various orders of H_{16}: natural order, quick-sort order in $d = 0.5, -0.5, 2$, and -2.

APPENDIX D: SIMULATIONS OF QUICK-SORT SPI SCHEME

To test the performance of the quick-sort scheme, some numerical simulations are performed. We introduce the peak signal-to-noise ratio (P_{SNR}) as the evaluation criterion, which is defined as

$$P_{\mathrm{SNR}} = 10 \log 10 \frac{255^2}{M_{\mathrm{SE}}}, \tag{D1}$$

where $M_{\mathrm{SE}} = 1/pq \sum_{i,j=1}^{p,q} [I_0(i,j) - \tilde{I}(i,j)]$ represents the mean square error between the original image and the reconstructed image; I_0 and $\tilde{I}$ represent the original image and the reconstructed image by the proposed scheme. p and q represent the number of pixels in the x and y directions. The higher the P_{SNR}, the better the reconstructed image quality.

As shown in Fig. 9(a), we use the OAM Bell-state $|\Psi^+\rangle$ numerical simulation image (64 × 64 pixels) as the original image, where $m = 3$ and $\theta = 0$. In simulation, the original image is under sampled and then the reconstructed images are obtained through TVAL3. Sampling ratio is defined as the ratio of sampling times to the total number of pixels in an image. The reconstruction results obtained

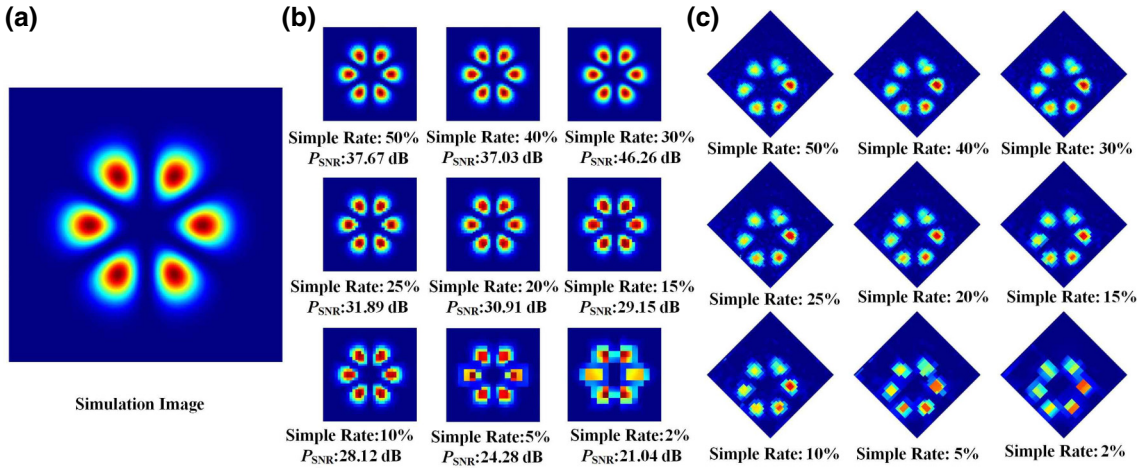

FIG. 9. The sampling ratio is determined by simulation and experiment. (a) The OAM Bell state of $m = 3$ and $\theta = 0$ generated by simulation (64 × 64 pixels). (b) In the simulation, the images reconstructed by TVAL3 at the sampling ratio of 50%, 40%, 30%, 25%, 20%, 15%, 10%, 5%, and 2% and parameter $d = 0.5$, the sampling ratios and P_{SNRs} are written at the bottom of each image. (c) In the experiment, the images reconstructed by TVAL3 use the same sampling ratio and d as in the simulation, the sampling ratios are written at the bottom of each image.

from the simulation with $d = 0.5$ and sampling ratio of 50%, 40%, 30%, 25%, 20%, 15%, 10%, 5%, and 2% are shown in Fig. 9(b). The corresponding reconstruction results obtained in the experiment are shown in Fig. 9(c). Based on the P_{SNR} of the reconstructed results in simulation and the intuitive resolution performance of the results in simulation and experiment, we select the lowest sampling rate as possible to reduce sampling time. Therefore, we select the parameter $d = 0.5$ with a sampling rate of 10% to collect experimental data.

[1] A. Einstein, B. Podolsky, and N. Rosen, Can quantum-mechanical description of physical reality be considered complete?, Phys. Rev. **47**, 777 (1935).

[2] P. G. Kwiat, E. Waks, A. G. White, I. Appelbaum, and P. H. Eberhar, Ultrabright source of polarization-entangled photons, Phys. Rev. A **60**, R773 (1999).

[3] Y. H. Kim, S. P. Kulik, and Y. H. Shih, Quantum Teleportation of Polarization State with a Complete Bell State Measurement, Phys. Rev. Lett. **86**, 1370 (2001).

[4] X. S. Ma, S. Zotter, J. Kofler, R. Ursin, T. Jennewein, C. Brukner, and A. Zeilinger, Experimental delayed-choice entanglement swapping, Nat. Phys. **8**, 479 (2012).

[5] Y. S. Kim, T. Pramanik, Y. W. Cho, M. Yang, S. W. Han, S. Y. Lee, M. S. Kang, and S. Moon, Informationally symmetrical Bell state preparation and measurement, Opt. Express **26**, 29539 (2018).

[6] A. Mair, A. Vaziri, G. Weihs, and A. Zeilinger, Entanglement of the orbital angular momentum states of photons, Nature (London) **412**, 313 (2001).

[7] Y. H. Kim, Single-photon two-qubit entangled states: Preparation and measurement, Phys. Rev. A. **67**, 040301 (2003).

[8] X. X. Chen, J. Z. Yang, X. D. Chai, and A. N. Zhang, Single-photon Bell state measurement based on a quantum random walk, Phys. Rev. A. **100(6)**, 042302 (2019).

[9] T. Li and G. L. Long, Quantum secure direct communication based on single-photon Bell-state measurement, New J. Phys. **22**, 063017 (2020).

[10] B. Li, Y. Cao, Y. H. Li, W. Q. Cai, W. Y. Liu, J. G. Ren, S. K. Liao, H. N. Wu, S. L. Li, L. Li, N. L. Liu, C. Y. Lu, J. Yin, Y. A. Chen, C. Z. Peng, and J. W. Pan, Quantum State Transfer over 1200 km Assisted by Prior Distributed Entanglement, Phys. Rev. Lett. **128**, 170501 (2022).

[11] L. Allen, M. W. Beijersbergen, R. J. C. Spreeuw, and J. P. Woerdanm, Orbital angular momentum of light and the transformation of Laguerre-Gaussian laser modes, Phys. Rev. A. **45**, 8185 (1992).

[12] H. He, M. E. J. Friese, N. R. Hbckenberg, and H. Rubinszteindunlop, Direct Observation of Transfer of Angular Momentum to Absorptive Particles from a Laser Beam with a Phase Singularity, Phys. Rev. Lett. **75**, 826 (1995).

[13] J. T. Barreiro, T. C. Wei, and P. G. Kwiat, Beating the channel capacity limit for linear photonic superdense coding, Nat. Phys. **4**, 282 (2008).

[14] J. Leach, B. Jack, J. Romero, M. R. Marte, R. W. Boyd, A. K. Jha, S. M. Barnett, S. F. Arnold, and M. J. Padgett, Violation of a Bell inequality in two-dimensional orbital angular momentum state-spaces, Opt. Express. **17**, 8287 (2009).

[15] B. Jack, A. M. Yao, J. Leach, J. Romero, S. F. Arnold, D. G. Ireland, S. M. Barnett, and M. J. Padgett, Entanglement of arbitrary superpositions of modes within two-dimensional orbital angular momentum state spaces, Phys. Rev. A. **81**, 043844 (2010).

[16] L. J. Kong, Y. N. Li, R. Liu, W. R. Qi, Q. Wang, Z. X. Wang, S. Y. Huang, Y. Si, C. H. Tu, W. Hu, F. Xu, Y. Q. Lu, and H. T. Wang, Complete measurement and multiplexing of orbital angular momentum Bell states, Phys. Rev. A. **100**, 023822 (2019).

[17] S. H. Ru, M. An, Y. Yang, R. Qu, F. R. Wang, Y. L. Wang, P. Zhang, and F. L. Li, Quantum state transfer between two photons with polarization and orbital angular momentum via quantum teleportation technology, Phys. Rev. A. **103**, 052404 (2021).

[18] M. Malik, M. Erhard, M. Huber, M. Krenn, R. Fickler, and A. Zeilinger, Multi-photon entanglement in high dimensions, Nat. Photonics **10**, 248 (2016).

[19] M. F. Duarte, M. A. Davenport, D. Takhar, J. N. Laska, T. Sun, K. Kelly, and R. G. Baraniuk, Single-pixel imaging via compressive sampling, IEEE Signal Process **25**, 83 (2008).

[20] Y. Bromberg, O. Katz, and X. Silberberg, Ghost imaging with a single detector, Phys. Rev. A. **79**, 053840 (2009).

[21] Z. B. Zhang, X. Ma, and J. G. Zhong, Single-pixel imaging by means of Fourier spectrum acquisition, Nat. Commun. **6**, 6225 (2015).

[22] J. Z. Yang, M. F. Li, X. X. Chen, W. K. Yu, and A. N. Zhang, Single-photon quantum imaging via single-photon illumination, Appl. Phys. Lett. **117**, 214001 (2020).

[23] G. A. Howland, D. J. Lum, M. R. Ware, and J. C. Howell, Photon counting compressive depth mapping, Opt. Express. **21**, 23822 (2013).

[24] P. A. Morris, R. S. Aspden, J. E. C. Bell, R. W. Boyd, and M. J.Padgett, Imaging with a small number of photons, Nat Commun. **6**, 5913 (2015).

[25] Z. B. Zhang, X. Y. Wang, G. A. Zheng, and J. G. Zhong, Hadamard single-pixel imaging versus Fourier single-pixel imaging, Opt. Express. **25**, 19619 (2017).

[26] A. X. Zhang, Y. H. He, L. A. Wu, L. M. Chen, and B. B. Wang, Tabletop x-ray ghost imaging with ultra-low radiation, Optica **5**, 374 (2018).

[27] M. J. Sun and J. M. Zhang, Single-pixel imaging and its application in three-dimensional reconstruction: A brief review, Sensors **19**, 732 (2019).

[28] M. J. Sun, L. T. Meng, M. P. Edgar, and N. A. Radwell, A Russian dolls ordering of the Hadamard basis for compressive single-pixel imaging, Sci. Rep. **7**, 3464 (2017).

[29] M. W. Beijersbergen, R. P. C. Coerwinkel, M. Kristensen, and J. P. Woerdman, Helical-wavefront laser beams produced with a spiral phaseplate, Opt Commun. **112**, 321 (1994).

[30] H. Walter, S. Bemet, M. Ritsch-Marte, I. Harder, and N. Lindlein, Adjustable difiractive spiral phase plates, Opt. Express. **23**, 413 (2015).

[31] N. R. Heckenberg, R. McDuff, C. P. Smith, and A. G. White, Generation of optical phase singularities

by computer-generated holograms, Opt. Lett. **17**, 221 (1992).

[32] C. Maurer, A. Jesacher, S. Furhapter, S. Bemet, and M. Ritsch-Marte, Tailoring of arbitrary optical vector beams, New J. Phys. **9**, 78 (2007).

[33] L. Marrucci, E. Karimi, S. Slussarenko, B. Piccirillo, E. Santamato, E. Nagali, and F. Sciarrino, Spin-to-orbital conversion of the angular momentum of light and its classical and quantum applications, J. Opt **13**, 064001 (2011).

[34] S. R. Nersisyan, N. V. Tabiryan, D. Mawet, and E. Serabyn, Improving vector vortex wave plates for high contrast coronagraphy, Opt. Express. **21**, 008205 (2013).

[35] Z. J. Zhang, L. Z. Cen, F. Wang, and Y. Zhao, Tiny velocity measurement using rotating petal-like mode of orbital angular momentum, Opt. Lett. **46**, 4805 (2021).

[36] W. K. Yu, Super sub-Nyquist single-pixel imaging by means of cake-cutting Hadamard basis sort, Sensors **19**, 4122 (2019).

[37] X. X. Chen, Z. Meng, J. Li, J. Z. Yang, A. N. Zhang, T. Kopyciuk, and P. Kurzynski, Nonclassical oscillations in pre- and post-selected quantum walks, Phys. Rev. A. **104**, 012220 (2021).